Supporting Information

Geyer et al. 10.1073/pnas.1300895110

A. Image Analysis

High-speed movies were analyzed using custom-made Matlab software (MathWorks Inc); our image analysis pipeline is illustrated in Fig. S1. In a first step, estimates for position and orientation of the cell body in a movie frame were obtained by a cross-correlation analysis using rotated template images. In a second step, these position and orientation estimates were refined by tracking the bright phase halo surrounding the cell. The first and second area moments of the cell rim provide accurate estimates for the center of the cell body and its long orientation axis. While the tracking precision of the first step amounts to <500 nm for the position and a few degrees for the orientation, these values are reduced to <50 nm and <0.5° after the second step, respectively. Special care was taken to reduce any potential bias of the flagellar phase on the cell-body tracking; for example, the cell rim close to the flagellar bases was obtained by interpolation instead of direct tracking. The flagellar base is visible as a continuous, parabola-shaped curve that connects the proximal ends of the two flagella; tracking of this flagellar base was done by a combination of line scans and local fitting of a Gaussian line model (step 3). Flagella were tracked by advancing along their length using exploratory line-scans in a successive manner (step 4). Flagellar tracking can be refined by local fitting of a Gaussian line model. A movie consisting of 1,000 frames can be analyzed in an automated manner within 10 h on a standard personal computer. Movies from red-light illumination conditions were of lower quality and required manual correction of the automated tracking results for each frame.

B. Flagellar Shape Analysis

We employ a nonlinear dimension reduction technique to represent tracked flagellar shapes as points in a low-dimensional abstract shape space. In a first step, smoothed tracked flagellar shapes corresponding to one cycle of synchronized flagellar beating (shown in Fig. 1*A*) were used to define the basis of the shape space. Flagellar shapes can be conveniently represented with respect to the material frame of the cell using a tangent angle representation (1, 2). In terms of this tangent angle $\theta(s)$, the $x(s)$ and $y(s)$ coordinates of the flagellar midline as functions of arclength s along the flagellum can be expressed as

$$x(s) = x(0) + \int_0^s d\xi \, \cos[\alpha + \theta(\xi)] \quad \text{and}$$
$$y(s) = y(0) + \int_0^s d\xi \, \sin[\alpha + \theta(\xi)]. \qquad \textbf{[S1]}$$

Here, α is the orientation angle of the long axis of the cell body (Fig. 1*A*), which implies that $\theta(\xi)$ characterizes flagellar shapes with respect to a material frame of the cell body. By averaging the tangent angle profiles $\theta(s,t)$ over a full beat cycle, we define a time-averaged flagellar shape characterized by a tangent angle $\overline{\theta}(s)$. To characterize variations from this mean flagellar shape, we employed a kernel principal component analysis (PCA) (3). The kernel used to compute the Gram matrix D for the kernel PCA must account for the 2π periodicity of the tangent angle data and was taken as $D_{ij} = \int_0^L ds \, \cos[\theta(s,t_i) - \theta(s,t_j)]$. The first three shape eigenmodes account for 97% of the spectrum of D and are shown in Fig. S2*A*. The relative contributions to the spectrum read 67% (first mode), 18% (second mode), and 12% (third mode). Whereas the first mode $\theta_1(s)$ (blue) describes nearly uniform bending of the flagellum, the second mode $\theta_2(s)$ (green) and the third mode $\theta_3(s)$ (red) together comprise the components of a traveling bending wave.

Next, any flagellar shape can be projected onto the shape space spanned by these three shape modes: Given a flagellar midline with coordinates $x(s)$ and $y(s)$, we seek the optimal approximating shape with coordinates $\hat{x}(s)$, $\hat{y}(s)$ whose tangent angle $\hat{\theta}(s)$ is a linear combination of the fundamental shape modes:

$$\hat{\theta}(s) = \overline{\theta}(s) + \beta_1\theta_1(s) + \beta_2\theta_2(s) + \beta_3\theta_3(s). \qquad \textbf{[S2]}$$

The coefficients β_1, β_2, and β_3 are obtained by a non-linear fit that minimizes the squared Euclidean distance $\int_0^{L'} ds |x(s) - \hat{x}(s)|^2 + |y(s) - \hat{y}(s)|^2$. This procedure is robust and works even if flagellar shapes could only be tracked partially with tracked length L' shorter than the total flagellar length L. Note that for nonsmoothed flagellar shapes the tangent angle representations can be noisy and are thus less suitable for fitting as compared to x, y coordinates.

A time sequence of tracked flagellar shapes thus results in a point cloud in the shape space parameterized by the shape mode coefficients β_1, β_2, and β_3. We fitted a closed curve to the torus-like point cloud (Fig. S2*B*, solid line). This closed curve represents a limit cycle of periodic flagellar beating. Each tracked flagellar shape can be assigned the "closest" point on this limit cycle (i.e., the point for which the corresponding flagellar shape has minimal Euclidean distance). By choosing a phase angle parameterization for the limit cycle, the phase angle of each flagellar shape is determined modulo 2π. A time-series of flagellar shapes thus yields a time-series of the flagellar phase angle $\varphi(t)$. The phase angle parameterization of the limit cycle had been chosen such that the flagellar phase angle φ and its time derivative are not correlated. Finally, the zero point $\varphi = 0$ was chosen such that the corresponding flagellar shape was nearly straight and perpendicular to the long cell axis.

C. Computation of Hydrodynamic Friction Forces

For our hydrodynamic computations, we represented a *Chlamydomonas* cell by an ensemble of $N = 300$ equally sized spheres of radius $a = 0.25$ μm. The cell body was chosen spheroidal and is represented by 272 spheres that are arranged in a symmetric fashion to retain mirror symmetries. Each flagellum is represented by a chain of 14 spheres that are aligned along a flagellar midline with equidistant spacing. The shapes of the flagellar midlines depend on respective phase angles φ_L and φ_R for the left and right flagellum. These flagellar shapes were taken from experiment for one full period of synchronized beating and are shown in Fig. 1*A*. We assume that the 272 spheres constituting the cell body move as a rigid sphere cluster. Each of the flagellar spheres represents a cluster with just one sphere, which results in a total of $n = 2 \cdot 14 + 1 = 29$ sphere clusters. We then computed the $6n \times 6n$ grand hydrodynamic friction matrix G for this ensemble of n spheres clusters using a freely available hydrodynamic library based on a Cartesian multipole expansion technique (4). Recall that the grand hydrodynamic friction matrix G relates the forces and torques exerted by the $6n$ sphere clusters to their translational and rotational velocities (5):

$$\mathrm{P}_0 = \mathrm{G} \cdot \dot{\mathrm{q}}_0. \qquad \textbf{[S3]}$$

Here, $\dot{\mathrm{q}}_0$ denotes a $6n$ vector that combines the translational and rotational velocity components of the n sphere clusters,

$$\dot{\mathrm{q}}_0 = (v_{1x}, v_{1y}, v_{1z}, \omega_{1x}, \omega_{1y}, \omega_{1z}, \ldots, \omega_{nz}), \qquad \textbf{[S4]}$$

whereas the $6n$ vector P_0 combines the components of the resultant hydrodynamic friction forces and torques,

$$\mathrm{P}_0 = \left(F_{1x}, F_{1y}, F_{1z}, T'_{1x}, T'_{1y}, T'_{1z}, \ldots, T'_{nz}\right). \qquad \textbf{[S5]}$$

(Primed torques represent torques with respect to the center of the respective sphere cluster.) Fig. 2*C* in the main text shows a submatrix of the grand friction matrix, which was defined as $G_{ij,yy} = G_{6i-4,6j-4}$, $i,j = 1, \ldots, n$. In this figure, it was assumed that the long cell body axis is aligned with the y axis of the laboratory frame (i.e., $\alpha = 0$), which implies that the submatrix relates motion in the direction of the long cell axis and the hydrodynamic force components projected on this axis.

For our hydrodynamic computations, the multipole expansion order was chosen as three. An estimate for the accuracy of our computation could be obtained by increasing the expansion order parameter, which changed the computed friction coefficients by less than 1%. Initial tests confirmed that the friction matrix of only the cell body gave practically the same result as the analytic solution for the enveloping spheroid (6); similarly, the computed friction matrix of only a single flagellum matched the prediction of resistive-force theory (7) assuming a flagellar radius equal to the sphere radius. Note that the precise value of the flagellar radius is expected to affect hydrodynamic friction coefficients only as a logarithmic correction (8).

Below, we consider an extension of the theoretical description given in the main text that additionally considers the possibility of an elastically anchored flagellar base, which allows for pivoting of the flagellar basal apparatus (Fig. S9). In this case, the flagellar midlines were rotated by an angle ψ.

A set of 2,400 precomputed configurations was then used to construct a spline-based lookup table of the (reduced) hydrodynamic friction matrix as a function of the degrees of freedom φ_L, φ_R, and ψ. The interpolation error was confirmed to be on the order of 1% or less. This lookup table was then used for the numerical integration of the (stiff) equations of motion, Eqs. **1** and **S17**.

D. Generalized Hydrodynamic Friction Forces

We employ the framework of Lagrangian mechanics of dissipative systems (9) to define generalized hydrodynamic friction forces and derive an equation of motion for the effective degrees of freedom in our theoretical description of *Chlamydomonas* swimming and synchronization. The $6n$ degrees of freedom q_0 for the n sphere clusters used in our hydrodynamic computations are enslaved by the five effective degrees of freedom in our coarse-grained theory (Fig. 1). Below, one more degree of freedom, ψ, is introduced to characterize pivoting of an elastically anchored flagellar basal apparatus. We thus have

$$\mathrm{q}_0 = \mathrm{q}_0(\mathrm{q}), \qquad \textbf{[S6]}$$

where we introduced the six-component vector $\mathrm{q} = (x, y, \alpha, \varphi_L, \varphi_R, \psi)$ that comprises the six effective degrees of freedom. The reduced 6×6 hydrodynamic friction matrix Γ for these six effective degrees of freedom can be computed from the grand hydrodynamic friction matrix G as

$$\Gamma = \mathrm{L}^T \cdot \mathrm{G} \cdot \mathrm{L} \qquad \textbf{[S7]}$$

with a $6n \times 6$ transformation matrix L given by refs. 10 and 11:

$$L_{ij} = \partial \dot{q}_{0,i} / \partial \dot{q}_j. \qquad \textbf{[S8]}$$

The rate of hydrodynamic dissipation can now be equivalently written as a quadratic function of either $\dot{\mathrm{q}}_0$ or $\dot{\mathrm{q}}$:

$$\mathcal{R} = \dot{\mathrm{q}}_0^T \cdot \mathrm{G} \cdot \dot{\mathrm{q}}_0 = \dot{\mathrm{q}}^T \cdot \Gamma \cdot \dot{\mathrm{q}}. \qquad \textbf{[S9]}$$

The generalized hydrodynamic friction coefficients Γ_{ij} are depicted in Fig. S3. In this context, generalized hydrodynamic friction forces can be defined as

$$P_j = \Gamma_{jx}\dot{x} + \Gamma_{jy}\dot{y} + \Gamma_{j\alpha}\dot{\alpha} + \Gamma_{jL}\dot{\varphi}_L + \Gamma_{jR}\dot{\varphi}_R + \Gamma_{j\psi}\dot{\psi}, \quad j = x, y, \alpha, L, R, \psi. \qquad \textbf{[S10]}$$

Interestingly, the generalized hydrodynamic friction force conjugated to one degree of freedom depends also on the rates of the change of the other degrees of freedom, which implies a coupling between the various degrees of freedom. This fact is illustrated by Fig. S4. Fig. S4*A* depicts the translational velocities of the flagellar spheres caused by pure yawing of the cell body with rate $\dot{\alpha}$. This motion is characterized by a $6n$ vector of velocity components, $\dot{\mathrm{q}}_0^{(\alpha)} = \mathrm{L} \cdot (0, 0, \dot{\alpha}, 0, 0, 0)^T$. Similarly, the beating of the left flagellum induces hydrodynamic friction forces as shown in Fig. S4*B*. The resultant force (and torque) components are combined in the $6n$ vector $\mathrm{P}_0^{(L)} = \mathrm{G} \cdot \mathrm{L} \cdot (0, 0, 0, \dot{\varphi}_L, 0, 0)^T$. Fig. S4 indicates that the scalar product $\dot{\mathrm{q}}_0^{(\alpha)} \cdot \mathrm{P}_0^{(L)} = \dot{\alpha}\Gamma_{\alpha L}\dot{\varphi}_L$ does not vanish, which implies a nonzero friction coefficient $\Gamma_{\alpha L}$ and thus a coupling between cell-body yawing and flagellar beating.

In our theoretical description, the phase dynamics of the left flagellum, say, is governed by a balance of the generalized hydrodynamic friction force P_L and an active driving force Q_L, similarly $Q_R = P_L$ for the right flagellum. In the case of free swimming, force and torque balance imply $P_x = P_y = 0$ and $P_\alpha = 0$. Together with an equation for P_ψ, these equation allow to self-consistently solve for the rate of change $\dot{\mathrm{q}}$ of the 6 degrees of freedom. If one degree of freedom were constrained, $q_j = 0$, the corresponding force equation becomes void, since a constraining force Q_j equal to P_j then balances the generalized hydrodynamic friction force P_j associated with this degree of freedom.

In general, the active driving forces Q_L and Q_R will depend on the flagellar phase. This phase dependence is fully determined by the requirement that the flagellar phase speeds should be constant, $\dot{\varphi}_j = \omega_0$, in the case of synchronized flagellar beating with $\delta = 0$. Here, ω_0 denotes the angular frequency of synchronized flagellar beating. Explicitly, we find

$$Q_L(\varphi_L) = \omega_0 \Big[\Gamma_{LL}(\varphi_L, \varphi_L) + \Gamma_{LR}(\varphi_L, \varphi_L) - 2\Gamma_{Ly}^2(\varphi_L, \varphi_L) / \Gamma_{yy}(\varphi_L, \varphi_L) \Big]. \qquad \textbf{[S11]}$$

An analogous expression holds for $Q_R(\varphi_R)$. Note that the generalized active driving forces are conjugate to an angle, and therefore have the physical unit piconewtons times micrometer. These phase-dependent active driving forces can be written as potential forces $Q_j = -\partial U / \partial \varphi_j$, $j = L, R$, where the potential U reads

$$U = -\int_{-\infty}^{\varphi_L} d\varphi_L Q_L(\varphi_L) - \int_{-\infty}^{\varphi_R} d\varphi_R Q_R(\varphi_R). \qquad \textbf{[S12]}$$

The potential U continuously decreases with time, indicating the depletion of an internal energy store and the dissipation of energy into the fluid during flagellar swimming. The rate of hydrodynamic dissipation equals the rate at which potential energy is dissipated:

$$\mathcal{R} = -\dot{U} = Q_L \dot{\varphi}_L + Q_R \dot{\varphi}_R. \qquad \textbf{[S13]}$$

E. Analytic Expression for the Flagellar Synchronization Strength

We present details on the derivation of Eqs. **5** and **6** for the synchronization strength λ in the case of the reduced equations of motion, Eqs. **2–4**. We assume equal intrinsic beat frequencies, $\omega_L = \omega_R = \omega_0$, and a small initial phase difference, $0 < \delta(0) \ll 1$. To leading order in δ, we find relations that link the rotation rate $\dot{\alpha}$ and the rate $\dot{\delta}$ at which the phase difference changes,

$$k\alpha + \rho(\varphi, \varphi)\dot{\alpha} = -d[\nu(\varphi)\delta]/dt \qquad \textbf{[S14]}$$

$$\dot{\delta} = -2\mu(\varphi)\dot{\alpha}. \qquad \textbf{[S15]}$$

Here $\varphi \approx \omega_0 t$ denotes the mean flagellar phase. The first equation describes how flagellar asynchrony causes a yawing motion of the cell body, and the second equation describes how this yawing motion then changes the flagellar phase difference. In the absence of any elastic constraint for yawing, $k = 0$, we can solve for $\dot{\delta}$:

$$(\rho - 2\mu\nu)\dot{\delta} = 2\mu\nu'\omega_0\delta. \qquad \textbf{[S16]}$$

Now, Eq. **5** follows from Eq. **S16** using $\lambda = -\int_0^T dt\, \dot{\delta}/\delta$ and a variable transformation $\varphi(t) = \omega_0 t + \mathcal{O}(\delta)$.

In the case of a very stiff elastic constraint with $k \gg \rho\omega_0$, we make use of the fact that variations of the phase difference δ during one beat cycle will be small compared to its mean value $\delta_0 = \langle\delta\rangle$. As a consequence, Eq. **S14** can be approximated as $k\alpha = -\nu'\omega_0\delta_0$. Using this approximation and Eq. **S15**, Eq. **6** follows.

F. Comparison of Experiment and Theory

We can compare instantaneous swimming velocities predicted by our hydrodynamic computation with experimental measurements and find favorable agreement (Fig. 3 and Fig. S5). Note that wall effects present in our experiments, but not accounted for by our hydrodynamic computations, are expected to reduce translational velocities (but less so rotational velocities) (12). The hydrodynamic computations are based on a fixed flagellar beat pattern parameterized by a flagellar phase angle, which was obtained experimentally for one beat cycle with synchronized beating (Fig. 1*A*). The good agreement between theoretical predictions and experimental measurements for the instantaneous swimming velocities further validate our reductionist description of the flagellar shape dynamics by just a single phase variable for each flagellum. Next, we tested the applicability of the reduced equations of motion, Eqs. **2–4**, in the experimental situation. For this aim, we reconstructed the coupling functions $\mu(\varphi)$, $\nu(\varphi)$ and $\rho(\varphi)$ from experimental time series data for $\dot{\alpha}$, $\dot{\varphi}_L$, and $\dot{\varphi}_R$. The coupling functions were represented by truncated Fourier series and the unknown Fourier coefficients determined by a linear regression of Eqs. **2**, **3**, or **4**, respectively (Fig. S6). Repeating this fitting procedure for data from six different cells gave consistent results (Fig. S7). Moreover, the phase dependence of the fitted coupling functions agrees qualitatively with our theoretical predictions. Note that our simple theory does not involve any adjustable parameters.

G. An Elastically Anchored Flagellar Basal Apparatus

In the main text, we had assumed for simplicity that the flagellar base is rigidly anchored to the cell body. Whereas the proximal segments of the two flagella are tightly mechanically coupled with each other by so-called striated fibers to form the flagellar basal apparatus, the flagellar basal apparatus itself is only connected to an array of 16 long microtubules spanning the cell (13). We now consider the possibility that this anchorage allows for some pivoting of the flagellar basal apparatus as a whole by an angle ψ (Fig. S9*A*). In addition to the 5 degrees of freedom of *Chlamydomonas* beating and swimming considered in the main text (Fig. 1), we now include this pivot angle ψ as a 6th degree of freedom. The rate of hydrodynamic dissipation is now given by $\mathcal{R} = \dot{x}P_x + \dot{y}P_y + \dot{\alpha}P_\alpha + \dot{\varphi}_L P_L + \dot{\varphi}_R P_R + \dot{\psi}P_\psi$, with P_ψ being the generalized hydrodynamic friction force conjugate to the pivot angle ψ. Assuming Hookean behavior for the elastic basal anchorage with rotational pivoting stiffness $\bar{k}$, we readily arrive at an equation of motion that reads in the case of free swimming:

$$(\dot{x}, \dot{y}, \dot{\alpha}, \dot{\varphi}_L, \dot{\varphi}_R, \dot{\psi})^T = \Gamma^{-1}\left(0, 0, 0, Q_L, Q_R, -\bar{k}\psi\right)^T. \qquad \textbf{[S17]}$$

Fig. S9*B* shows flagellar synchronization for a free-swimming cell with elastically anchored flagellar base: Although some basal pivoting occurs as a result of flagellar asynchrony, the swimming and synchronization behavior is very similar to the case of a rigidly anchored flagellar base, as shown in Fig. 4*A*. For a cell that can neither translate nor yaw, however, the situation is different (Fig. S9*C*). We find strong flagellar synchronization provided the elastic stiffness $\bar{k}$ is not too large. Flagellar synchronization by basal pivoting is thus effective also for a fully clamped cell. In contrast, for a rigidly anchored flagellar base, the synchronization strength λ would be relatively weak in this case, being due only to direct hydrodynamic interactions between the two flagella.

Flagellar synchronization by basal pivoting is conceptually very similar to synchronization by cell-body yawing as discussed in the main text. In the case of a fully clamped cell, we can approximate the synchronization dynamics by virtually the same generic equation of motion as Eqs. **2–4**, when we substitute ψ for α:

$$\dot{\varphi}_L = \omega_0 - \bar{\mu}(\varphi_L)\dot{\psi}, \qquad \textbf{[S18]}$$

$$\dot{\varphi}_R = \omega_0 + \bar{\mu}(\varphi_R)\dot{\psi}, \qquad \textbf{[S19]}$$

$$\bar{k}\psi + \bar{\rho}(\varphi_L, \varphi_R)\dot{\psi} = -\bar{\nu}(\varphi_L)\dot{\varphi}_L + \bar{\nu}(\varphi_R)\dot{\varphi}_R. \qquad \textbf{[S20]}$$

Here, the coupling functions $\bar{\mu}$, $\bar{\nu}$, and $\bar{\rho}$ play a similar role as the previously defined μ, ν , and ρ for Eqs. **2–4** and show a qualitatively similar dependence on the flagellar phase (Fig. S10). To derive Eqs. **S18–S20**, we neglected direct hydrodynamic interactions between the two flagella and approximated the active driving forces by $Q_L(\varphi) = \omega_0\Gamma_{LL}(\varphi, \varphi)_{|\psi=0}$ and $Q_R(\varphi) = \omega_0\Gamma_{RR}(\varphi, \varphi)_{|\psi=0}$. The coupling functions are defined as $\bar{\mu}(\varphi) = -\Gamma_{L\psi}(\varphi, \varphi)/\Gamma_{LL}(\varphi, \varphi)_{|\psi=0}$, $\bar{\nu}(\varphi) = -\Gamma_{\psi L}(\varphi, \varphi)_{|\psi=0}$, and $\bar{\rho}(\varphi, \varphi) = \Gamma_{\psi\psi}(\varphi_L, \varphi_R)_{|\psi=0}$. This choice retains the key nonlinearities of the full equation of motion (Fig. S3). Eq. **S18** states that pivoting of the flagellar basal apparatus with $\dot{\psi} > 0$ slows down the effective stroke of the left flagellum (and speeds up the right flagellum). For synchronized flagellar beating, there will be no pivoting of the flagellar base. For asynchronous beating, however, the flagellar base will be rotated out of its symmetric rest position by an angle ψ if the stiffness $\bar{k}$ is not too large. Any pivoting motion of the flagellar base during the beat cycle changes the hydrodynamic friction forces that oppose the flagellar beat, which in turn can either slow down or speed up the respective flagellar beat cycles, and thus restore flagellar synchrony.

To gain further analytical insight, we study the response of the dynamical system in Eqs. **S18–S20** after a small perturbation $0 < \delta(0) \ll 1$. To leading order in $\delta = \varphi_L - \varphi_R$, we find (with $\varphi \approx \omega_0 t$)

$$\bar{k}\psi + \rho(\varphi, \varphi)\dot{\psi} = -d[\bar{\nu}(\varphi)\delta]/dt, \qquad \textbf{[S21]}$$

$$\dot{\delta} = -2\bar{\mu}(\varphi)\dot{\psi}. \qquad \textbf{[S22]}$$

In the biologically relevant case of a relatively stiff basal anchorage of the flagellar basal apparatus with $\overline{k} \gg \rho\omega_0$, we find for the synchronization strength a result analogous to Eq. **6**:

$$\overline{\lambda} = -\oint_0^{2\pi} d\varphi \;\; \frac{\overline{\mu}(\varphi)\overline{\nu}''(\varphi)}{\overline{k}/\omega_0}. \qquad \textbf{[S23]}$$

1. Riedel-Kruse IH, Hilfinger A, Howard J, Jülicher F (2007) How molecular motors shape the flagellar beat. *HFSP J* 1(3):192–208.
2. Friedrich BM, Riedel-Kruse IH, Howard J, Jülicher F (2010) High-precision tracking of sperm swimming fine structure provides strong test of resistive force theory. *J Exp Biol* 213(Pt 8):1226–1234.
3. Scholkopf B, Smola AJ, Bernhard S (2002) *Learning with Kernels: Support Vector Machines, Regularization, Optimization, and Beyond* (*Adaptive Computation and Machine Learning*) (MIT, Cambridge, MA).
4. Hinsen K (1995) HYDR0LIB : A library for the evaluation of hydrodynamic interactions in colloidal suspensions. *Comput Phys Commun* 88:327–340.
5. Happel J, Brenner H (1965) *Low Reynolds Number Hydrodynamics* (Kluwer, Boston).
6. Perrin F (1934) Mouvement Brownien d'un ellipsoide (I). Dispersion diélectrique pour des molécules ellipsoidales. *J Phys Radium* 7:497–511.
7. Gray J, Hancock GT (1955) The propulsion of sea-urchin spermatozoa. *J Exp Biol* 32:802–814.
8. Brennen C, Winet H (1977) Fluid mechanics of propulsion by cilia and flagella. *Annu Rev Fluid Mech* 9:339–398.
9. Goldstein H, Poole C, Safko J (2002) *Classical Mechanics* (Addison-Wesley, Reading, MA), 3rd Ed.
10. Friedrich BM, Jülicher F (2012) Flagellar synchronization independent of hydrodynamic interactions. *Phys Rev Lett* 109(13):138102.
11. Polotzek K, Friedrich BM (2013) A three-sphere swimmer for flagellar synchronization. *New J Phys* 15:045005.
12. Bayly PV, et al. (2011) Propulsive forces on the flagellum during locomotion of Chlamydomonas reinhardtii. *Biophys J* 100(11):2716–2725.
13. Ringo DL (1967) Flagellar motion and fine structure of the flagellar apparatus in Chlamydomonas. *J Cell Biol* 33(3):543–571.

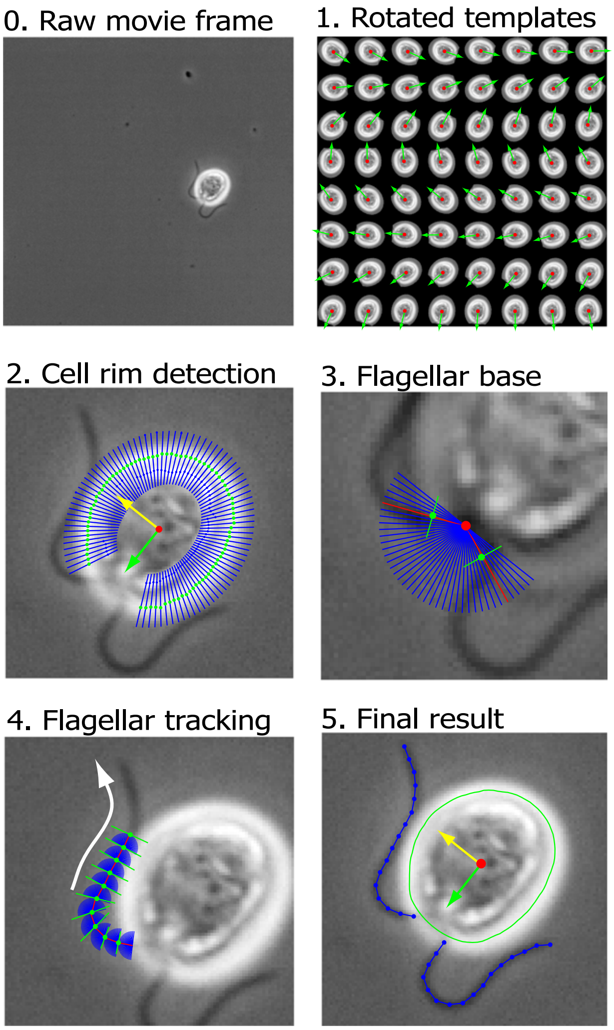

Fig. S1. Image analysis pipeline used to automatically track planar cell position and orientation as well as flagellar shapes in high-speed movies of swimming *Chlamydomonas* cells. (*0*) A typical movie frame. (*1*) Rotated template images used for a cross-correlation analysis to estimate cell position and orientation in a movie frame. (*2*) The cell body outline was tracked by detecting intensity maxima (green) of line scans along rays (shown in blue), which emanate from the putative cell-body center. From the cell-body outline, we obtain refined estimates for cell position and orientation. (*3*) The position of the flagellar base was then determined using a fan of line scans (along the blue lines), followed by a line scan (green) in a direction perpendicular to the maximal intensity direction (red). (*4*) Finally, flagellar shapes were tracked in a successive manner using combinations of line scans similar to those in step 3. (*5*) The final result of our tracking software provides for each frame: cell body position (red dot) and orientation (green arrow), cell body rim (green), as well as center lines of the two flagella (blue).

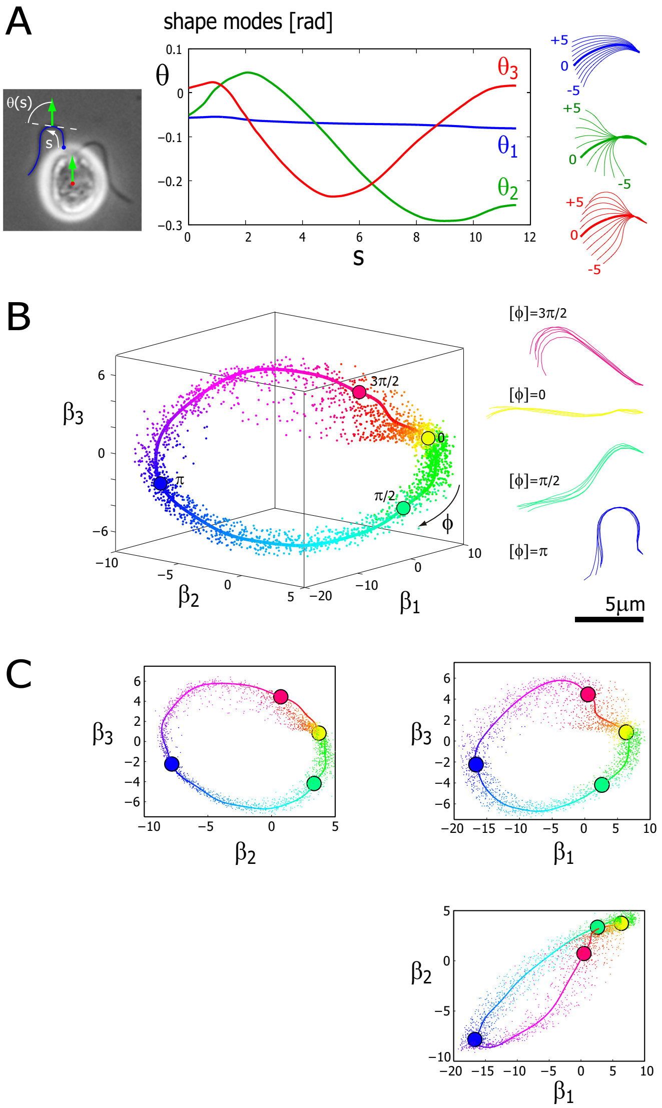

Fig. S2. We represent a single flagellar shape by $n = 3$ shape coefficients as a point in an abstract shape space that is spanned by three principal shape modes. (*A*) The principal shape modes were determined by employing a kernel PCA to the tangent angle representation $\theta(s)$ of smoothed flagellar shapes that were tracked from the left flagellum of cell no. 2 during one beat cycle of synchronized flagellar beating. From the PCA, we obtained three dominant shape modes with respective tangent angle representations $\theta_1(s)$, $\theta_2(s)$, and $\theta_3(s)$ as shown. Together, these principal shape modes account for 97% of the variance of this tangent angle dataset. For sake of illustration, exemplary flagellar shapes corresponding to the superposition of the mean flagellar shape and just one shape mode with tangent angle $\overline{\theta}(s) + \beta_i\theta_i(s)$, $i = 1,2,3$ are shown to the right $(-5 \leq \beta_i \leq 5)$. (*B*) Each tracked flagellar shape from one flagellum can be represented by a single point in an abstract shape space that is spanned by the three principal shape modes. More specifically, the coordinates $(\beta_1, \beta_2, \beta_3)$ of this point are obtained by approximating the tracked flagellar shape by a superposition of a previously computed mean flagellar shape and the three principal shape modes (Eq. **S2**). The set of flagellar shapes from an entire experimental movie thus corresponds to a point cloud. This point cloud scatters around a closed curve (solid line), which reflects the periodic nature of the flagellar beat. This closed curve has been obtained by a simple fit to the point cloud of flagellar shapes and can be considered as a limit cycle of flagellar beating. Deviations from this limit cycle measure the variability of the flagellar beat. We can use this representation to define a distinct flagellar phase angle φ (modulo 2π) for each tracked flagellar shape as indicated by the color code by mapping each flagellar shape onto the limit cycle. A time series of flagellar shapes thus yields a time series of the flagellar phase angle $\varphi(t)$. As an illustration of this assignment, superpositions of flagellar shapes are shown to the right, each of which corresponds to flagellar shapes that were assigned the same flagellar phase modulo 2π. (*C*) Two-dimensional projections corresponding to the three-dimensional shape space representation in *B*.

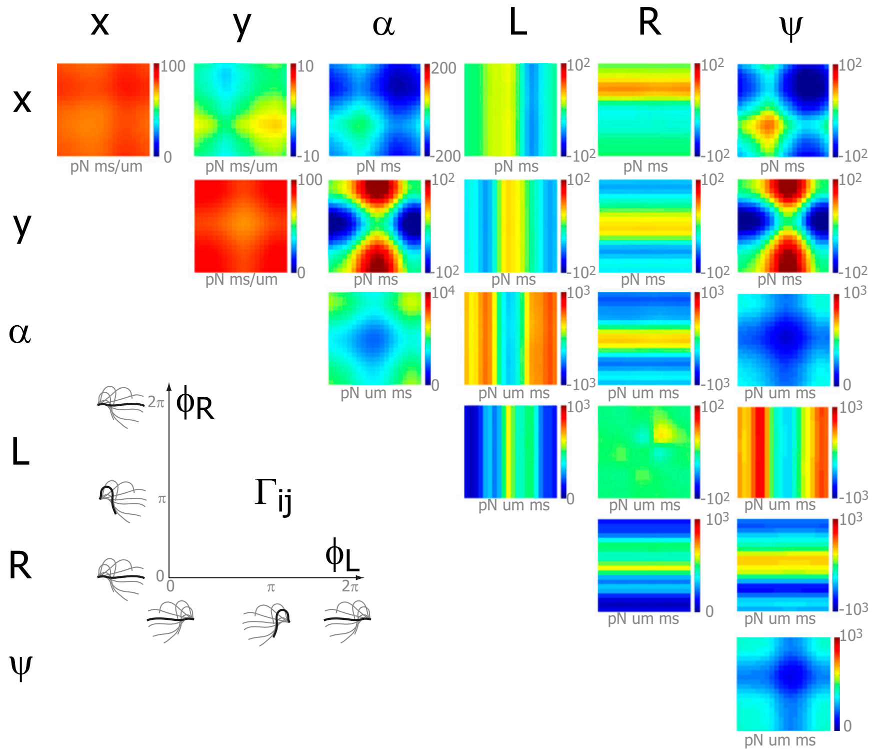

Fig. S3. Generalized hydrodynamic friction matrix Γ_{ij} associated with the effective degrees of freedom x, y, α, φ_L, φ_R, and ψ. This generalized friction matrix determines the generalized hydrodynamic friction forces P_i conjugate to the degrees of freedom $\mathrm{q}=(x,y,\alpha,\varphi_L,\varphi_R,\psi)$ as $P_i=\Gamma_{ij}\dot{q}_j$, and is computed as a projection of the grand hydrodynamic friction matrix (Eq. **S7**). Each friction coefficient Γ_{ij} is a periodic function of the two phase angles φ_L and φ_R, $\Gamma_{i,j}=\Gamma_{i,j}(\varphi_L,\varphi_R)$ and is represented as a color plot with axes as indicated. Here, α is set to zero; different values of α would correspond to a simple rotation of the matrix shown. By Onsager symmetry, $\Gamma_{ij}=\Gamma_{ji}$. Several features are noteworthy. The coefficient Γ_{LR} characterizes hydrodynamic interactions between the two flagella and is found to be small compared to, for example, Γ_{LL}. The other coefficients $\Gamma_{Lj}=\Gamma_{jL}$, which set the friction force P_L conjugate to φ_L, depend strongly on φ_L, but almost not on φ_R. This is yet another manifestation of the fact that direct hydrodynamic interactions between the two flagella are comparably weak. Analogous statements hold for the coefficients Γ_{Rj}. A counter-clockwise rotation of the cell, $\dot{\alpha}>0$, will increase the friction force P_L during the effective stroke of the left flagellum $(\Gamma_{L\alpha}>0)$ but decrease the corresponding respective friction force P_R for the right flagellum during its effective stroke $(\Gamma_{R\alpha}<0)$. Mirror symmetry of the swimmer amounts to invariance of the friction matrix under the substitution $(x,y,\alpha,\varphi_L,\varphi_R)\rightarrow(-x,y,-\alpha,\varphi_R,\varphi_L)$, which implies a number of symmetry relations, for example, $\rho=\Gamma_{\alpha\alpha}$ must be symmetric in φ_L and φ_R. Finally, this rotational friction coefficient $\rho=\Gamma_{\alpha\alpha}$ depends on the flagellar phases in a more pronounced way than the translational friction coefficients Γ_{xx} and Γ_{yy}. This is in line with the general fact that rotational friction coefficients depend more strongly (as $\sim l^3$) on the effective linear dimension l of an object than translational friction coefficients $(\sim l)$. The coefficients $\Gamma_{j\alpha}$ and $\Gamma_{j\psi}$ associated with yawing of the whole cell and pivoting of the flagellar apparatus, respectively, show a similar dependence on the flagellar phases.

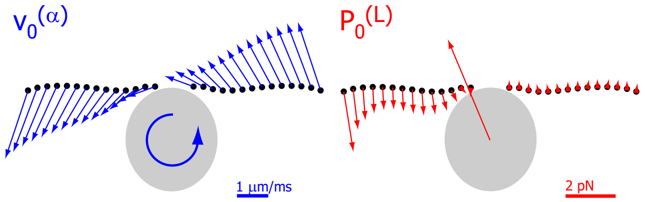

Fig. S4. Coupling of cell-body yawing and flagellar beating. (*Left*) Translational velocities of the flagellar spheres used in our hydrodynamic computation associated with a pure yawing motion of the cell body with rate $\dot{\alpha}$. (*Right*) Hydrodynamic friction forces exerted by the flagellar spheres (as well as by the cell body), if the left flagellum advances along its beat cycle with rate $\dot{\varphi}_L$. The generalized hydrodynamic friction coefficient $\Gamma_{\alpha L}$ that couples cell-body yawing and beating of the left flagellum can be computed as a scalar product between the velocity profile resulting from yawing and the force profile resulting from flagellar beating and is found to be non-zero. Parameters: $\dot{\varphi}_L=\omega_0$, $\dot{\alpha}=0.2\omega_0$, and $2\pi/\omega_0=30$ ms.

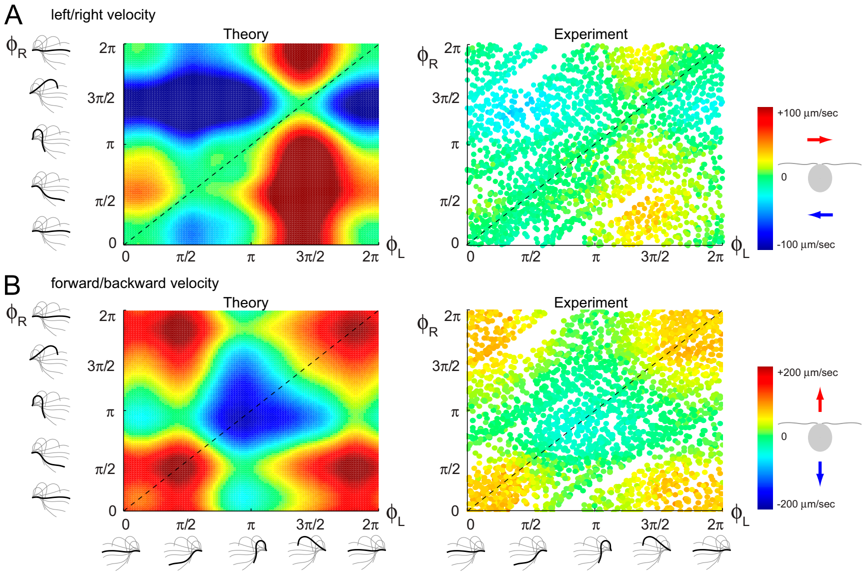

Fig. S5. (*A*) Instantaneous swimming velocity in the direction perpendicular to the long cell axis as a function of the flagellar phase angles φ_L and φ_R. For synchronized flagellar beating (dashed line), this velocity vanishes in our theory for symmetry reasons (green). If the two flagella are out of synchrony, however, significant sideward motion of the cell is observed, both in theory and experiment. Note that wall effects present in the experiments, but not considered in the computations, reduce translational velocities. (*B*) Instantaneous swimming velocity in the direction of the long cell axis, again as a function of the flagellar phase angles.

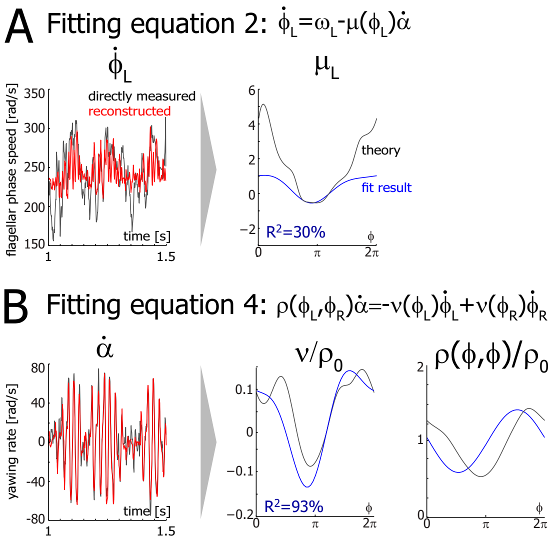

Fig. S6. The reduced equations of motion, Eqs. **2**–**4**, were fitted to experimental time-series data for the yawing rate $\dot{\alpha}$ of the cell, as well as the flagellar phase speeds $\dot{\varphi}_L$ and $\dot{\varphi}_R$. This provided experimental estimates for the phase-dependent coupling functions μ, ν, and ρ. Specifically, we represented each coupling function as a truncated Fourier series and determined the unknown Fourier coefficients by a linear regression using Eqs. **2**–**4**. (*A*) Linear regression of Eq. **2**. Shown to the left in black is the instantaneous flagellar phase speed of the left flagellum $\dot{\varphi}_L$ (smoothed with a span of 15 ms). Shown in red is a reconstructed phase speed $\omega_L-\mu_L(\varphi_L)\dot{\alpha}$ that depends on the instantaneous cell-body yawing rate $\dot{\alpha}$, as well as the intrinsic flagellar frequency ω_L and phase-dependent coupling function μ_L for the left flagellum, which were obtained by the fit. The coefficient of determination was $R^2=30\%$. The estimate for μ_L obtained from this fit is shown to the right (blue), together with a theoretical prediction (black) (see also Fig. 5*A*). (*B*) Linear regression of Eq. **4**. Shown to the left is the measured instantaneous yawing rate $\dot{\alpha}$ of the cell body (black) and a yawing rate reconstructed from the flagellar phase dynamics, $[-\nu(\varphi_L)\dot{\varphi}_L+\nu(\varphi_R)\dot{\varphi}_R]/\rho(\varphi_L,\varphi_R)$ (red). The coefficient of determination was $R^2=93\%$. From this fit, we obtain an experimental estimate for the coupling functions $\nu(\varphi)$ and $\rho(\varphi_L,\varphi_R)$ (blue); theoretical predictions are shown in black.

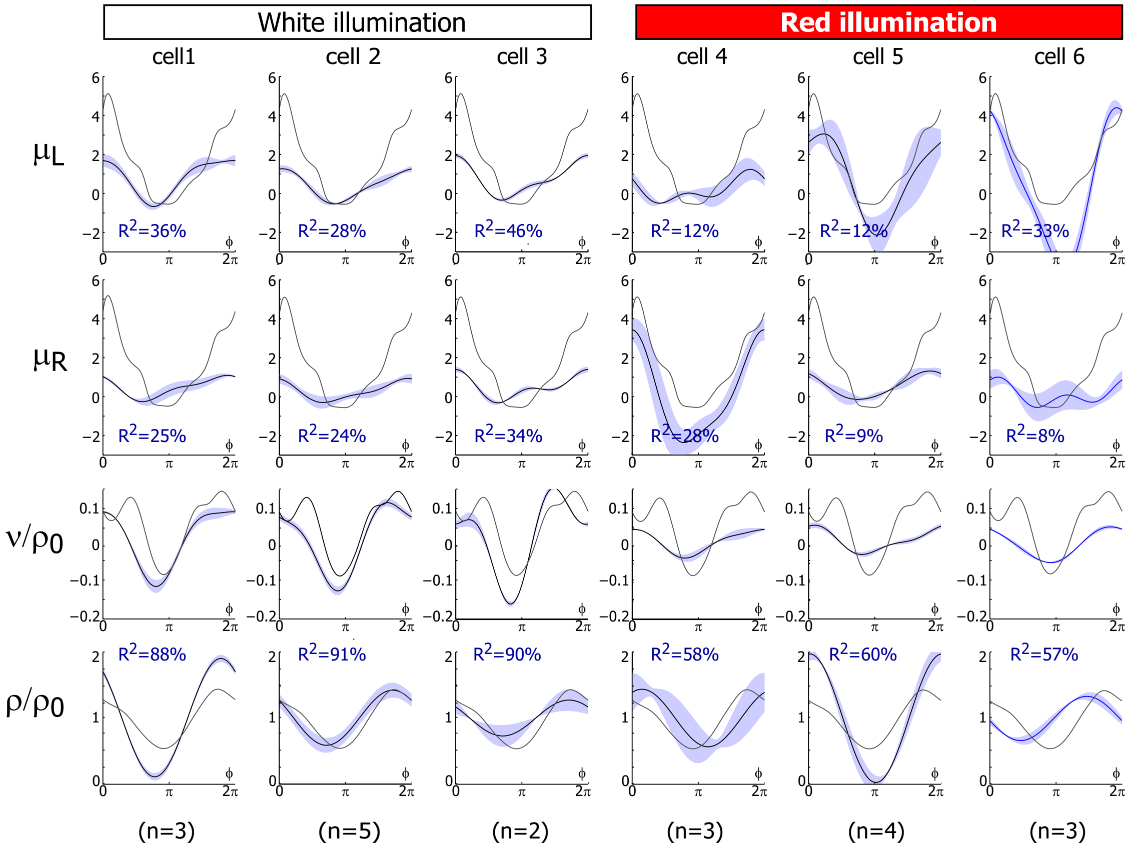

Fig. S7. Experimental fits for the coupling functions μ, ν, and ρ introduced in Eqs. **2–4** (blue curves, shaded regions indicate mean ± SE) and theoretical predictions (black). The coupling functions μ, ν, and ρ relate flagellar beating and cell-body yawing. Fitting results are shown for six different cells illuminated by either white or red light as indicated. For each cell, we employed n fits using n nonoverlapping time series of duration 0.4–0.5 s with n as indicated. The blue curves represent the average of the fitted coupling functions for the n fits; the averaged coefficient of determination R^2 is stated.

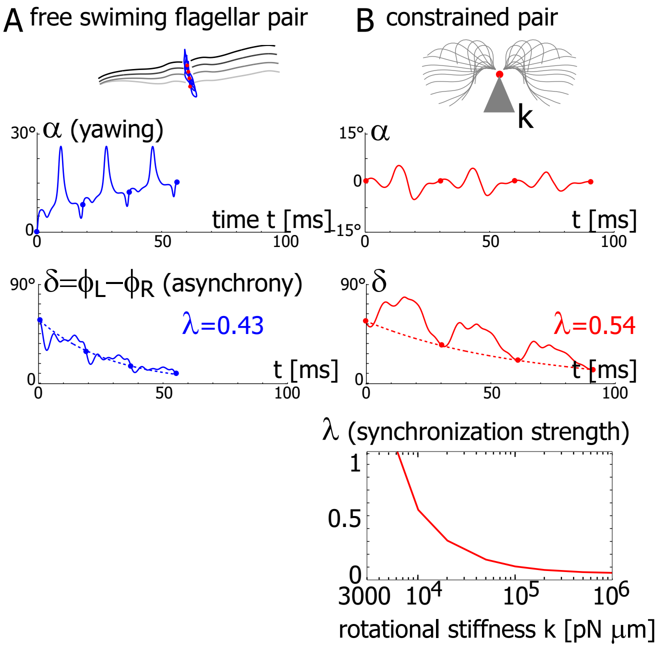

Fig. S8. Theory of flagellar synchronization for an isolated flagellar pair. Inspired by experiments by Hyams and Borisy (1) reporting synchronization in isolated flagellar pairs, we computed the swimming and synchronization behavior of a flagellar pair with cell body removed. For the computations, we used flagellar shapes and flagellar driving forces $Q_j(\varphi)$, $j=L,R$, determined from an intact cell (Fig. 1) (*A*) For a free-swimming flagellar pair, we observe a characteristic yawing motion of the flagellar pair characterized by $\alpha(t)$, if the two flagella are initially out of synchrony. The flagellar phase difference δ is found to decrease with time (solid line), approximately following an exponential decay (dotted line). This implies that the in-phase synchronized state is stable with respect to perturbations. Each completion of a full beat cycle of the left flagellum is marked by a dot. (*B*) To mimic experiments in which external forces constrain the motion of the flagellar pair, we simulated the idealized case of a pair that cannot translate, while yawing of the pair is constricted by an elastic restoring torque $Q_\alpha=-k\alpha$ that acts at the basal apparatus (red dot). As in the case of a free-swimming pair, the flagellar phase difference δ decays with time, indicating stable synchronization. In the case of a constrained cell, the synchronization strength λ strongly depends on the clamping stiffness k. Parameters: $2\pi/\omega_0=30$ ms, $k=10^4$ pN µm/rad. To enhance numerical stability, we added a small constant $\kappa=10$ pN µm ms to the flagellar friction coefficients, $\Gamma_{jj}(\varphi_L,\varphi_R)$, $j=L,R$, which corresponds to internal dissipation (2).

1. Hyams JS, Borisy GG (1975) Flagellar coordination in *Chlamydomonas reinhardtii*: isolation and reactivation of the flagellar apparatus. *Science* 189(4206):891–893.
2. Friedrich BM, Jülicher F (2012) Flagellar synchronization independent of hydrodynamic interactions. *Phys Rev Lett* 109(13):138102.

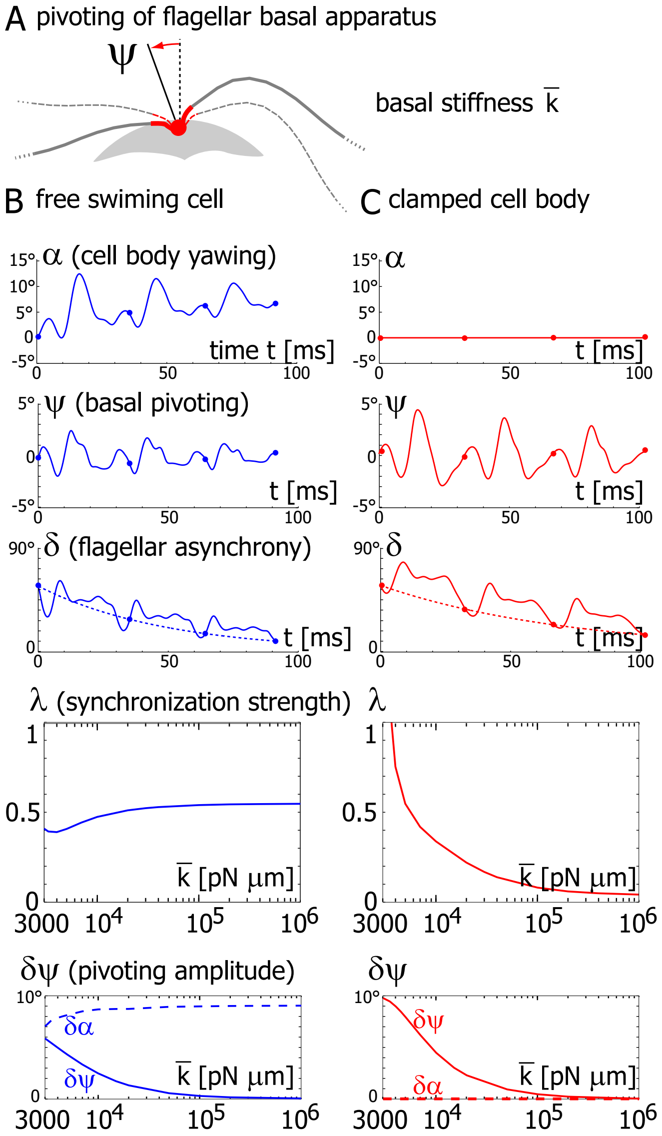

Fig. S9. Theory of flagellar synchronization by basal pivoting. (*A*) We consider the possibility of an elastically anchored flagellar basal apparatus (red), which allows for pivoting of the basal apparatus (solid lines) by an angle ψ from its symmetric reference configuration (dashed lines). (*B*) For a free-swimming cell, the equation of motion, Eq. **S17**, predicts both a yawing motion of the cell characterized by $\alpha(t)$ and a pivoting motion of the flagellar base characterized by $\psi(t)$, if the two flagella are initially out of synchrony. The flagellar phase difference δ is found to decrease with time (solid line), approximately following an exponential decay (dotted line). This implies that the in-phase synchronized state is stable with respect to perturbations. Each completion of a full beat cycle of the left flagellum is marked by a dot. The synchronization behavior in the case of an elastically anchored flagellar basal apparatus is nearly identical to the case of a stiff anchorage, as shown in the main text in Fig. 4. The lowest panel shows typical amplitudes of basal pivoting ($\delta\psi$, solid line) and cell-body yawing ($\delta\alpha$, dashed line) as a function of basal stiffness $\overline{k}$. Amplitudes were determined as half the range of variation during one beat cycle for an initial phase difference of $\delta(0) = \pi/2$. (*C*) For a clamped cell that can neither translate nor rotate, the flagellar apparatus can still pivot and will do so if the two flagella are initially out of phase. As in the case of a free-swimming cell, the flagellar phase difference δ decays with time, indicating stable synchronization. In the case of a clamped cell, the synchronization strength λ strongly depends on the stiffness $\overline{k}$ of the elastic anchorage of the basal flagellar apparatus, which sets the amplitude of basal pivoting. Parameters: $2\pi/\omega_0 = 30$ ms, $\overline{k} = 10^4$ pN μm/rad.

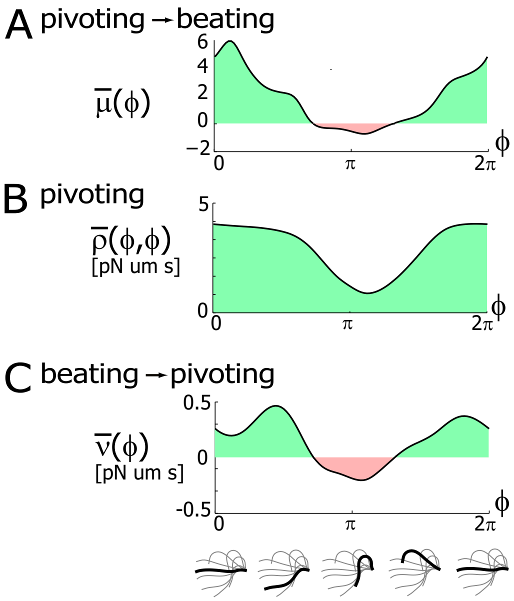

Fig. S10. Theoretical coupling functions for the case of a pivoting flagellar base. (*A*) A pivoting motion of the flagellar base changes the hydrodynamic friction force associated with flagellar beating and thereby speeds up or slows down the flagellar beat cycle in our theory. This effect is quantified by a coupling function $\bar{\mu}$ (Eq. **S18**). (*B*) Hydrodynamic friction associated with pivoting of the flagellar base (and the attached flagella) is characterized by a friction coefficient $\bar{\rho}$ (Eq. **S20**). This friction coefficient is maximal when the two flagella extend maximally from the cell body during their effective stroke. (*C*) The beat of the left flagellum causes pivoting of the flagellar base. This effect is quantified by a coupling function $\bar{\nu}$ (Eq. **S20**).